Journal of Catalysis 275 (2010) 270–279

Contents lists available at ScienceDirect

Journal of Catalysis

journal homepage: www.elsevier.com/locate/jcat

Microkinetic modeling of spatially resolved autothermal CH_4 catalytic partial oxidation experiments over Rh-coated foams

A. Donazzi [a], M. Maestri [a], B.C. Michael [b], A. Beretta [a,*], P. Forzatti [a], G. Groppi [a], E. Tronconi [a], L.D. Schmidt [b], D.G. Vlachos [c]

[a] Laboratory of Catalysis and Catalytic Processes, Dipartimento di Energia, Politecnico di Milano, piazza Leonardo da Vinci 32, 20133 Milano, Italy
[b] Department of Chemical Engineering and Materials Science (CEMS), University of Minnesota, 432 Amundson Hall, 421 Washington Avenue SE, Minneapolis, MN 55455, USA
[c] Department of Chemical Engineering and Center for Catalytic Science and Technology (CCST), University of Delaware, Newark, DE 19716-3110, USA

ARTICLE INFO

Article history:
Received 19 April 2010
Revised 3 August 2010
Accepted 16 August 2010
Available online 16 September 2010

Keywords:
Catalytic partial oxidation
Methane
Rhodium
Microkinetic model
Spatial profiles
Transport phenomena

ABSTRACT

Spatially resolved autothermal experiments of CH_4 catalytic partial oxidation (CPO) performed over Rh-coated foams were analyzed using a detailed reactor model and a novel, thermodynamically consistent C_1 microkinetic scheme. The effect of depositing Rh (5 wt%) on an 80 ppi α-Al_2O_3 foam directly or after washcoating with γ-Al_2O_3 washcoat (2 wt%) was examined. For the first time, a fully predictive approach was adopted in the numerical analysis by introducing in the model the experimentally estimated catalyst metal surface area and state of the art correlations for heat and mass transfer in foams. Characterization of the catalysts by H_2 pulse chemisorption and SEM microscopy revealed that the washcoat addition increased the metal area by almost one order of magnitude, from 74 cm^2/g_{Foam} on Rh foams to 630 cm^2/g_{Foam} on washcoated foams. The numerical results showed that the model is able to quantitatively account for the axial evolution of the species and the temperature profiles of the solid and the gas phase within the catalyst volume. In line with previous results, it was confirmed that the consumption of O_2 is strictly governed by mass transfer and that the co-presence of O_2 and syngas in the bulk of the gas phase is exclusively due to mass transfer limitations. Reaction path analysis showed that CH_4 is activated via pyrolytic decomposition and its main oxidizer is OH^* and not O^*, both in the oxidation zone and in the reforming zone of the catalyst. By application of the most up-to-date experimental and numerical tools, the present results provide a clear picture of CH_4 CPO and emphasize the importance of modeling spatially resolved experiments in order to properly interpret the high density of information that these kinds of data provide.

1. Introduction

The catalytic partial oxidation of methane (CH_4 CPO, Eq. (1)) at short contact times (10^{-2}–10^{-4} s) is a fast, autothermal process suitable for selectively producing H_2 and CO in simple, compact reactors [1].

$$CH_4 + 1/2O_2 \rightarrow CO + 2H_2 \quad \Delta H_R^0 = -37\ \text{kJ mol}^{-1} \tag{1}$$

CH_4 CPO is ideal for small and medium scale applications, such as distributed and on-board production of H_2 and synthesis gas, either to feed fuel cells [2] or to assist engine and after-treatment applications [3]. Due to the small catalyst volumes and the high throughput, the reaction occurs with sharp gradients of temperature and concentration encompassing a strong interaction between chemical kinetics and transport phenomena. Understanding this interplay is crucial for the rational design of a CPO reformer in terms of internal layout, catalytic materials and geometry of the support. This calls for advanced modeling and experimental techniques. On the one hand, experimental measurement of these gradients allows to better rationalize the outcome of the process and to handle the thermal stresses, which can reduce catalyst life [4,5] and limit the extension of the CPO toward higher hydrocarbons. On the other hand, the development of reliable, chemically physically consistent models allows to engineer the process and to gain insights into the complexity of the experiments.

Recently, Schmidt and co-workers [6] developed a novel sampling technique that allows the measurement of spatially resolved temperature and concentration profiles within lab-scale CPO reformers operating under autothermal conditions. Substantial work has been done on CPO of CH_4 over Rh- and Pt-based catalysts over a wide set of experimental conditions [6–11]. The spatially resolved experiments provide higher density information than typical integral data collected at the outlet of a reactor. Nonetheless, their interpretation is complex due to the superposition of a number of phenomena. Consequently, comprehensive

* Corresponding author. Fax: +39 0223993318.
E-mail address: alessandra.beretta@polimi.it (A. Beretta).

0021-9517/$ - see front matter © 2010 Elsevier Inc. All rights reserved.
doi:10.1016/j.jcat.2010.08.007

Nomenclature

A	reactor cross section (m^2)
a_v	specific area per unit volume (m^{-1})
$\widehat{C}_P$	specific heat ($J\,kg^{-1}\,K^{-1}$)
f	friction factor
G	superficial mass flow rate ($kg\,m^{-2}\,s^{-1}$)
h	heat transfer coefficient ($W\,m^{-2}\,K^{-1}$)
k_{ax}	solid thermal conductivity ($W\,m^{-1}\,K^{-1}$)
k_{mat}	mass transfer coefficient ($m\,s^{-1}$)
L_{rct}	mass transfer coefficient (m)
p	pressure (Pa)
r	reaction rate ($mol\,kg_{cat}^{-1}\,s^{-1}$)
s	production rate ($mol\,cm^{-2}\,s^{-1}$)
t	time (s)
T	temperature (K)
z	reactor axial coordinate (m)

Greek symbols

ε	void fraction
ε_S	emissivity
σ	Stefan–Boltzmann constant ($W\,m^{-2}\,K^{-4}$)
θ	coverage site fraction
Γ	site density ($mol\,cm^{-2}$)
ξ	volumetric catalytic fraction
ρ	density ($g\,cm^{-3}$)
ω	weight fraction
ΔH^R	heat of reaction ($J\,mol^{-1}$)

Subscripts and superscripts

g	gas phase
s	solid phase
eff	effective
i	ith species
j	jth reaction

models are necessary. Toward this goal, Horn et al. [12] first proposed a numerical study of spatially resolved CH_4 CPO experiments performed over Rh-coated 80 ppi α-Al_2O_3 foams at different flow rates (5 and 10 slpm) and C/O ratios (0.7–1.3). Dalle Nogare et al. [13] further refined this analysis by comparing with measured solid temperature and by introducing mass and heat transport correlations for foam supports. These two numerical studies adopted the same kinetic scheme developed by Deutschmann and co-workers, which comprises 38 surface reactions [14]. Recently, Maestri et al. [15] have presented a comprehensive reaction mechanism of the CH_4 CPO process. In particular, they used fundamental surface chemistry [16] in combination with detailed reactor modeling [17] for the microkinetic analysis of quasi-isothermal CPO experiments in an annular reactor [15,18]. This analysis revealed that the interplay between mass transfer and surface chemistry is crucial in dictating the dominant reaction pathways leading to syngas. The partial oxidation of methane does not proceed according to reaction (1) [15]. Rather, it is a combination of different processes, with up to three reaction zones: deep combustion of methane first, followed by a zone where direct formation of syngas in parallel with catalytic combustion of product hydrogen occurs, and finally a steam reforming (SR) and water–gas shift (WGS) zone, when oxygen is no longer available. The extent of these zones underscores the importance of the interplay of transport phenomena and surface chemistry, pointing out that an accurate description of transport effects is required for a proper simulation of CPO data.

In this work, we present a fully predictive, microkinetic analysis of CH_4 CPO spatially resolved experiments on Rh-based foams with and without addition of washcoat prior to the metal deposition [10]; we address in detail both transport and chemical phenomena. First, we perform a morphological characterization of the foam in order to determine the pore diameter and the geometrical area. The characterization of the catalysts allowed us to estimate the metal surface area. Using these data as input, we have then performed microkinetic analysis of the experiments, combining the microkinetic model [16] with a 1D heterogeneous reactor model [19,20]. Our approach provides insight into the complexity of the experiments and enables fundamental understanding of the underlying phenomena at different time and space scales. In addition, it allows validation of model predictions against data with different metal surface area.

2. Experimental and theoretical tools

2.1. Operating conditions and catalytic materials

The autothermal CH_4 CPO experiments were performed over two different Rh catalysts, 5 wt% Rh and 5 wt% Rh/2 wt% γ-Al_2O_3 (hereafter referred to as Rh and Rh-wc) supported over 80 ppi α-Al_2O_3 foams (11 mm long, 17 mm diameter). In the case of the Rh sample, 5 wt% Rh was added directly on the foam by dropwise deposition of a $Rh(NO_3)_3$ solution. In the case of the Rh-wc sample, prior to the dropwise addition of Rh, the foam was washcoated with 2 wt% γ-Al_2O_3 (3 μm powders, 120 m^2/g surface area) by dropwise deposition of an aqueous slurry.

Both catalysts were tested under autothermal conditions, at atmospheric pressure, with a total flow rate of 5 slpm and gas mixtures consisting of 20% v/v CH_4, O/C ratio of 1 and Ar to balance. The gases were preheated at 150 °C. The reaction was light-off by heating the catalyst up to 400 °C with a $Ar/H_2/O_2$ diluted mixture and successively switching to the CH_4 CPO feed. Only steady-state profiles are presented.

The setup used for collecting spatially resolved concentration and temperature profiles is extensively described in [11]. The system consisted of an externally insulated quartz reactor equipped with a spatial sampling apparatus. The reactor mounted the catalytic foam in between two blank foams acting as heat shields. The sampling system consisted of a capillary of small diameter (550 μm) that was moved within a channel (∅ = 760 μm) axially drilled into the foams. The capillary was sealed at one end and connected to a linear actuator at the other end. The gases were sampled through a small orifice (~200 μm) cut close to the sealed head of the capillary and pumped to an analysis system, which included a mass spectrometer and a gas chromatograph.

For the measurement of the axial temperature profile of the gas and the solid phase, the reactor was equipped with a K-type thermocouple (∅ = 250 μm) and with a narrow-band infrared pyrometer (Impac Infrared, IGA 5-LO). The pyrometer consisted of a measuring transducer connected to an optical fiber (∅ = 330 μm) with a 45° polished tip. Indeed, as reported in [21], optical fibers with a 45° polished tip predominantly admit the radiation perpendicular to the central axis, opposite to the beveled surface. Contrarily to fibers with flat tips, the accepted radiation from surfaces in front is minimized.

Table 1
Model equations and boundary conditions [19,20].

Gas phase	
Mass balance	$\frac{\partial \omega_i}{\partial t} = -\frac{G}{\rho_g \cdot \varepsilon} \cdot \frac{\partial \omega_i}{\partial z} - \frac{a_v}{\varepsilon} \cdot k_{mat,i} \cdot (\omega_i - \omega_{i,wall}) + \frac{Diff_i}{\varepsilon} \cdot \frac{\partial \omega_i^2}{\partial z^2}$
Energy balance	$\frac{\partial T_g}{\partial t} = -\frac{G}{\rho_g \cdot \varepsilon} \cdot \frac{\partial T_g}{\partial z} - \frac{a_v \cdot h \cdot (T_g - T_S)}{\varepsilon \cdot \rho_g \cdot \widetilde{C}_{P,g}}$
Momentum balance	$\left(-\frac{1}{\rho_g} + \frac{G^2}{\rho_g^2 p}\right) \cdot \frac{dp}{dz} - \frac{G^2}{\rho_g^2 \cdot T_g} \cdot \frac{dT_g}{dz} = \frac{1}{2} \cdot \frac{G^2}{\rho_g^2} \cdot a_v \cdot f$
Solid phase	
Mass balance	$0 = a_v \cdot \rho_g \cdot k_{mat,i} \cdot (\omega_i - \omega_{i,wall}) + \left(\sum_{j=1}^{NR} v_{i,j} \cdot r_j^{eff}\right) \cdot MW_i \cdot \rho_s \cdot \xi$
Energy balance	$\frac{\partial T_s}{\partial t} = \frac{a_v \cdot h \cdot (T_g - T_s)}{\rho_s \cdot \widetilde{C}_{p,s} \cdot (1-\varepsilon)} + \frac{1}{\rho_s \cdot \widetilde{C}_{p,s}} \cdot \frac{\partial}{\partial z}\left(k_{ax}^{eff} \frac{\partial T_s}{\partial z}\right) + \left(\sum_{j=1}^{NR}\left(-\Delta H_j^R\right) \cdot r_j^{eff}\right) \cdot \frac{\xi}{\widetilde{C}_{p,s} \cdot (1-\varepsilon)}$
Site balance	$\frac{d\theta_i}{dt} = \frac{s_i}{\Gamma_{Rh}}$
Boundary conditions	
Reactor Inlet ($z_1 = 0$)	Reactor Outlet ($z_2 = L_{rct}$)
$\omega_{i,z=z_1} = \omega_{i,feed}$	$-k_{ax}^{eff} \cdot \frac{\partial T_s}{\partial z}\big\vert_{z_2} = -\sigma \cdot \varepsilon_s \cdot \left(T_g^4 - T_s^4\vert_{z_2}\right)$
$T_{g,z=z_1} = T_{IN} p_{z=z_1} = p_{feed}$	
$-k_{ax}^{eff} \cdot \frac{\partial T_s}{\partial z}\big\vert_{z_1} = \sigma \cdot \varepsilon_S \cdot \left(T_g^4 - T_S^4\vert_{z_2}\right)$	
Initial conditions	
$\omega_i(z,0) = 0, \quad T_g(z,0) = T_{room}, \quad T_s(z,0) = 400\ ^\circ C$	

The measuring transducer included the lens system, the IR detector and the signal processor. The IR detector was an Indium–Gallium–Arsenic photodiode, sensitive to radiation in the wavelength range 1.45–1.8 μm. The output voltage was calibrated between 350 and 1100 °C. The optical fiber was used as a probe for transmitting the radiation from the internal part of the reactor to the measuring transducer. Either the thermocouple or the optical fiber was inserted into the capillary, which provided an inert sleeve for the axial movements.

2.2. Reactor model and kinetic scheme

The experiments were analyzed by means of a 1D, heterogeneous, dynamic, fixed bed reactor model [19,20]. The model consists of mass, energy and momentum balances for the gas phase and the solid phase, which includes axial convection and diffusion, solid conduction and gas–solid transport terms (Table 1). However, under the investigated flow conditions, the contribution of the axial mass diffusion was found negligible. Gas-phase reactions were accounted for using the detailed scheme of Frassoldati et al. [22]. In line with Ref. [23], no contribution from homogeneous chemistry was found under our operating conditions. Heat conduction in the solid was described with an effective axial thermal conductivity coefficient for isotropic open-cellular foams [24] corrected by the addition of radiation [19]. The thermal conductivity of the α-Al_3O_3 support was taken as 2 W/m/K [12]. Radiative dispersion effects at the back and front heat shield were introduced in the boundary conditions. In agreement with the experimental procedure, the reactor light-off was simulated starting from a 400 °C catalyst up to the reaching of the steady state.

The model incorporates a thermodynamically consistent single site C_1 microkinetic scheme [16,25] for the conversion of CH_4 to syngas over Rh, consisting of 82 surface reactions and 13 adspecies. It has been derived using a hierarchical multiscale methodology involving both semi-empirical methods (UBI-QEP) and first principle techniques [16,26]. The scheme was validated over a wide set of CH_4 CPO experimental data within an annular microreactor under quasi-isothermal conditions [27,28]. The resulting scheme was able to describe several reacting systems, namely CH_4 pyrolysis and oxidation, steam reforming, H_2- and CO-rich oxidation, WGS and reverse WGS.

Modeling of temperature and concentration profiles within the catalysts requires heat and mass transfer correlations. State-of-the-art correlations were adopted, namely those derived by Incera Garrido et al. [29] for α-Al_2O_3 foams with pore density ranging between 10 and 45 ppi. According to the correlations, the following equation was used for mass transfer:

$$Sh = 1.000 \cdot Re^{0.47} \cdot Sc^{1/3} \cdot \left(\frac{D_P}{0.0001m}\right)^{0.58} \cdot \varepsilon^{0.44} \tag{2}$$

Given the Sherwood number (Eq. (2)), the Nusselt number for heat transfer was obtained by applying the Chilton–Colburn analogy. Concerning the geometric area of the foams, Incera Garrido et al. [29] proposed an empirical relation (Eq. (3)) derived on the basis of magnetic resonance imaging (MRI) analysis of their samples.

$$a_v = 3.84 \cdot D_p^{-0.85} \cdot \varepsilon^{-0.82} \tag{3}$$

As apparent from these equations, the void fraction ε and the pore diameter D_P must be experimentally determined.

3. Results

3.1. Morphological characterization of the foams

In terms of void fraction ε and pore diameter D_P, 80 ppi α-Al_2O_3 foams were characterized (Table 2). The void fraction was calculated according to the following equation:

$$\varepsilon = 1 - \frac{\rho_{Foam}}{\rho_{HS}} \tag{4}$$

The density of the hollow struts ($\rho_{HS} \sim 3.4$ g/cm^3) was estimated with a standard pycnometry method, based on the measurement of the buoyancy of the samples in pure ethanol

Table 2
Characterization of the foam support.

	Weight (g)	Diameter (mm)	Length (mm)	Pore size (μm)	ε (%)	Geometric area (cm^2/g)
80 ppi α-Al_2O_3	2.5	17	11	600	70	28

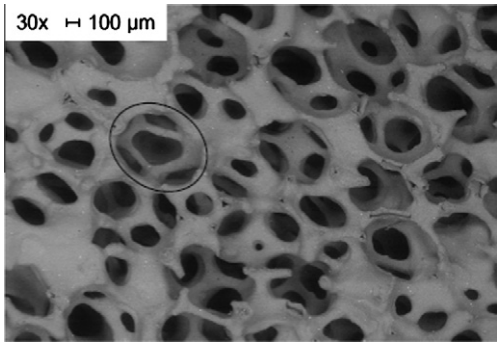

Fig. 1. SEM micrograph of an 80 ppi α-Al_2O_3 blank foam.

(Sartorius YDK 01). The apparent density of the foam (ρ_{Foam}) is the ratio of the weight of the foam sample (~2.5 g) and its geometrical volume (~2.5 cm^3). The void fraction is 70%.

The pore diameter was estimated by analysis of SEM micrographs (Fig. 1). Only isotropic pores located at the same depth were taken as representative, by accounting for the equatorial diameter of the cells (as shown in the figure). The pore diameter was calculated by averaging 50 measurements and was equal to 600 μm, in reasonable agreement with the value of 500 μm found in previous work in similar 80 ppi α-Al_2O_3 foams [7]. The measured pore diameter is much higher than the nominal one (~317 μm), estimated from the ppi characteristics given by the manufacturer. However, it is widely understood that the classification of foams by their ppi should not be taken literally [30], especially in the case of highly irregular structures. The nominal ppi given by the manufacturer is generally smaller than the experimental one, as apparent in a number of works [7,29,31,32].

As a consequence of the irregular distribution of the pore network, the determination of the geometric area of a foam is not a straightforward task. Fig. 1 shows that the coalescence of the cells resulted in blind cavities and thick struts with large accumulation of alumina. According to the correlation adopted (Eq. (3)), the geometric area was 28 cm^2/g_{Foam}, somewhat lower than the estimates used on the same kind of foams, namely 80 cm^2/g_{Foam} (cubic cell assumption) in [13] and 72 cm^2/g_{Foam} in [33].

3.2. Catalyst characterization

The characterization of the catalysts was performed after exposure to the reaction, so that the results were representative of the surface present during the CPO experiments.

Concerning the oxidation state of the surface, XRD spectra of the samples (not reported) exclusively revealed metal Rh and no detectable traces of Rh oxide.

In the case of Rh samples, the metal area was estimated from SEM micrographs (Fig. 2a–c), as it was too small to be accurately determined by H_2 pulse chemisorption. The micrographs show that the α-alumina surface was almost completely covered with Rh (Fig. 2a). In line with [34], a wide variety of aggregates was found (Fig. 2b and c), with dimensions ranging between 0.1 and 15 μm. By performing a volume average (Eq. (5)) on the different distributions of the particles size, a diameter of 3.3 μm was estimated, which corresponded to a Rh dispersion of 0.035% under the approximation of spherical aggregates. Given this value of dispersion, a metal surface area of 74 cm^2/g_{Foam} was determined, i.e. of the same order of magnitude of the geometric surface of the support.

$$d_{volume} = \frac{\sum_i^{NP} n_i \cdot d_i^4}{\sum_i^{NP} n_i \cdot d_i^3} \tag{5}$$

The estimation of the surface metal area of Rh-wc samples was carried out with H_2 pulse chemisorption (5% H_2 in Ar v/v, 25 °C), according to a standard procedure described in Ref. [35]. The surface metal area was 630 cm^2/g_{Foam} (0.3% Rh dispersion), nearly nine times higher than that of non-washcoated samples. This result is consistent with the beneficial effect of adding a washcoat, which, even in small amounts, increases the metal dispersion and reduces

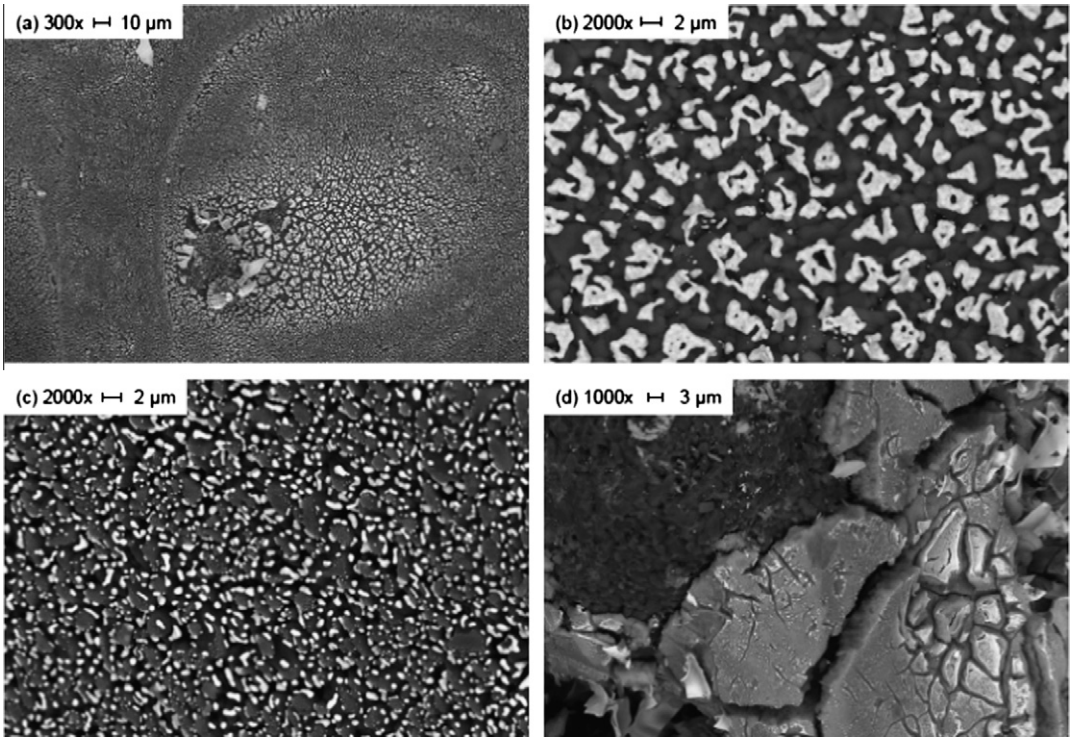

Fig. 2. SEM micrographs of the catalysts. Panels a–c: 5 wt% Rh supported on 80 ppi α-Al_2O_3 foam. Panel d: 5 wt% Rh/2 wt% γ-Al_2O_3 supported on 80 ppi α-Al_2O_3 foam.

sintering [33]. SEM micrographs (Fig. 2d) reveal that the washcoat was not homogenously dispersed over the surface of the foam, but rather it was present as irregular patches ~5 μm thick. Such a thin layer did not significantly alter the pore diameter of the foam. The measured thickness is consistent with the theoretical value of 7 μm, calculated by assuming a density of 1 g/cm^3 for the washcoat and a geometric area of 28 cm^2/g$_{Foam}$. Backscattering electron images (not reported) confirmed that part of Rh filled the washcoat layer. However, due to the low amount of washcoat, in some zones the excess of Rh formed a thin crust and was also found on the uncoated α-alumina surface.

3.3. Model simulations for the Rh catalyst

Fig. 3 compares model simulations and experimental results in the case of the Rh catalyst. Overall, the model predictions are satisfactory. Good agreement is found for the axial evolution of CH_4 (Panel a) and the outlet molar flows of the species (Table 3). The evolution of O_2 appears to be correctly described in terms of consumption rate up to the first millimeter of the catalyst. Afterward, between 1 and 1.8 mm, the data show a sharp drop in the O_2 molar flow up to the complete consumption, while the simulations tend to overestimate the length of the oxidation zone.

Panels b and c show the evolution of the products. In agreement with transport limitations in O_2 [15], H_2 and CO are formed in the oxidation zone, along with CO_2 and H_2O. Indeed, in the absence of O_2 at the wall, reforming reactions occur on the catalyst surface. In the oxidation zone, some deviations are apparent between data and simulations: H_2 and CO_2 are overestimated, while H_2O is underestimated. The model predicts a peak in the production of CO_2, which is absent in the experimental curve. Also, it does not predict the peak observed in the evolution of H_2O. The experiments indicate that, in this zone, WGS is not equilibrated and likely suggests that the C_1 scheme overpredicts the WGS activity of Rh. In the second part of the monolith, where O_2 is totally consumed and syngas is produced by CH_4 steam reforming, the simulations correctly describe the local composition. Due to the low metal dispersion, the evolution of the product composition significantly deviates from the equilibrium up to the outlet of the reactor.

The temperature profiles for the gas and the solid phase are reported in Panel d. In the oxidation zone, a significant difference between the gas and the catalyst temperature is observed. In the

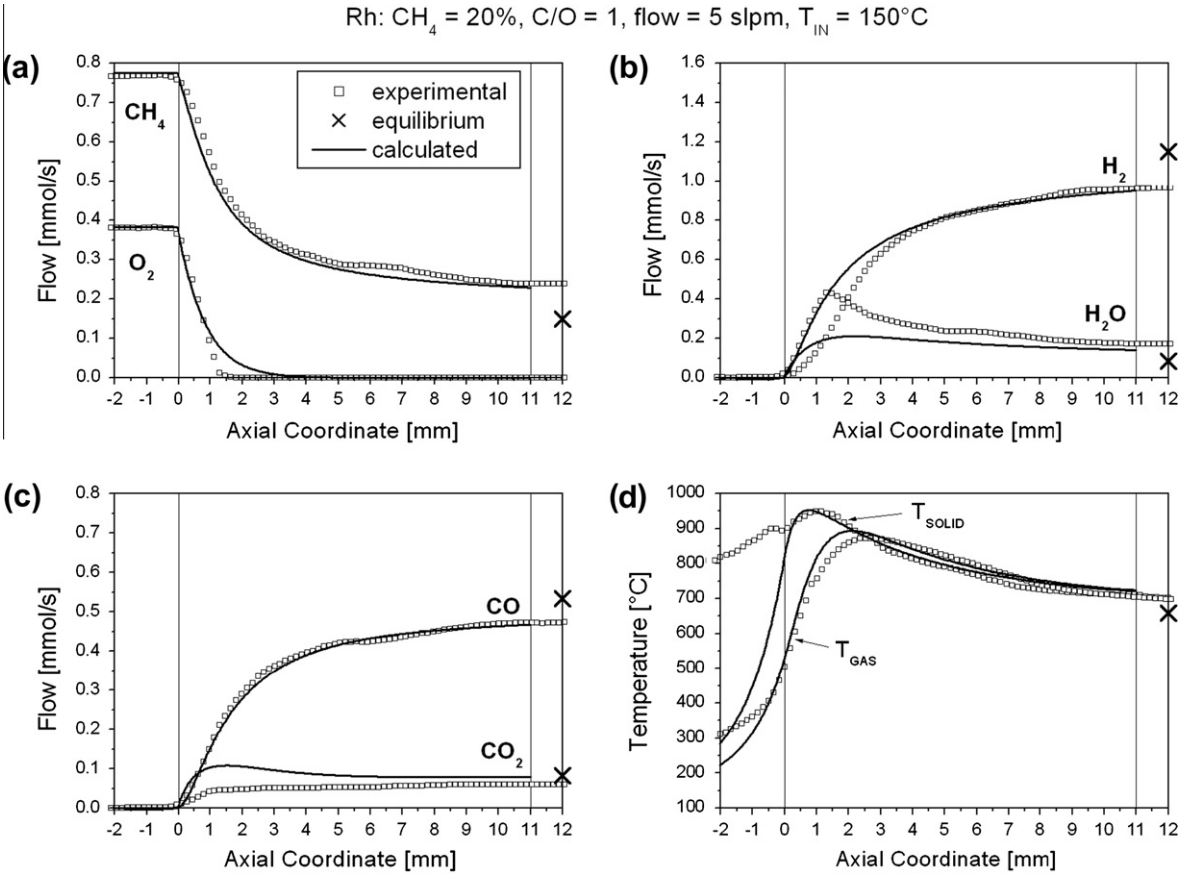

Fig. 3. Comparison between model prediction (solid lines) and data (symbols) for a CH_4 CPO experiment over the 5% Rh catalyst. Operating conditions: CH_4 = 20% v/v, O/C = 1, Flow = 5 slpm, T_{IN} = 150 °C, P = 1 atm. Panel a: CH_4 and O_2 flow rates. Panel b: H_2 and H_2O flow rates. Panel c: CO and CO_2 flow rates. Panel d: gas and surface temperature profiles.

Table 3
5 wt% Rh/α-Al_2O_3 catalyst: comparison between experimental and calculated outlet molar flows and temperature.

	CH_4 (mmol/s)	H_2 (mmol/s)	CO (mmol/s)	H_2O (mmol/s)	CO_2 (mmol/s)	T_{OUT} (°C)
Exp.	0.24	0.96	0.47	0.17	0.06	709
Calc.	0.23	0.95	0.47	0.14	0.08	704

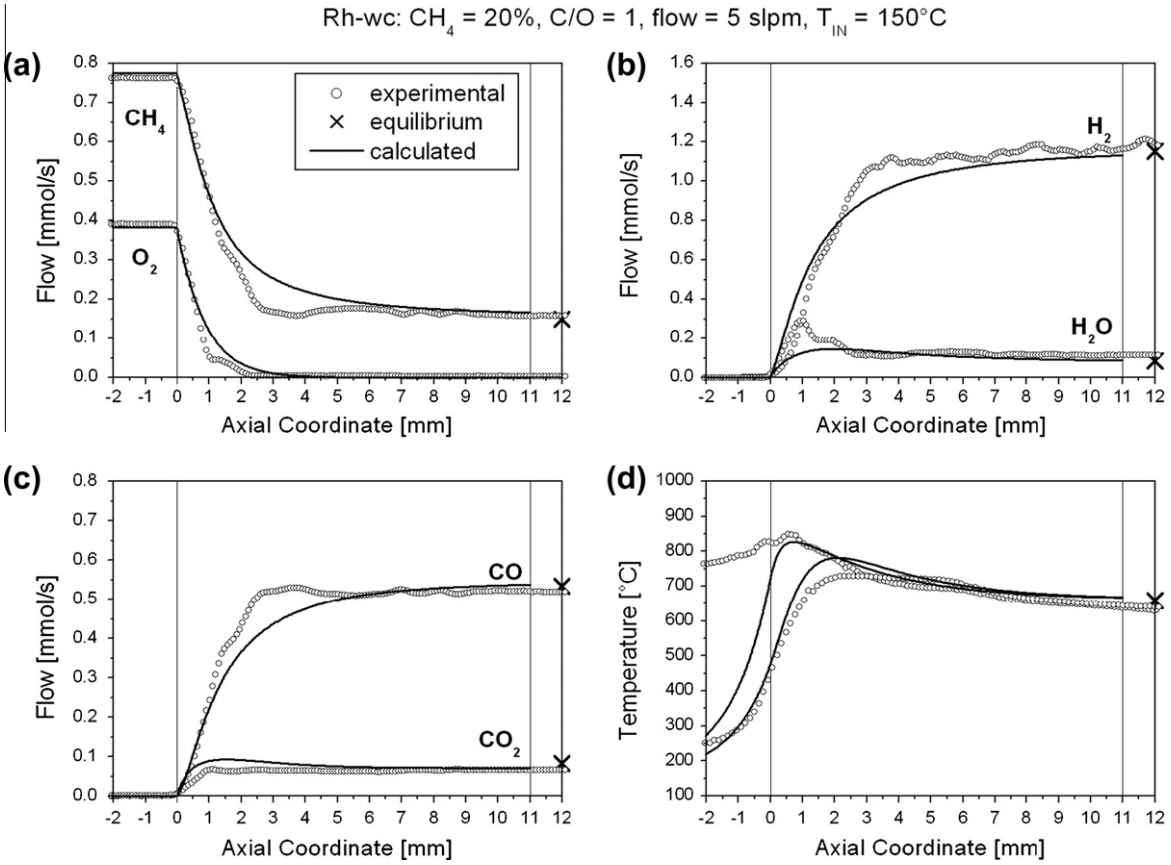

Fig. 4. Comparison between model prediction (solid lines) and data (symbols) for a CH_4 CPO experiment over the 5 wt% Rh/2 wt% γ-Al_2O_3 catalyst. Operating conditions: CH_4 = 20% v/v, O/C = 1, Flow = 5 slpm, T_{IN} = 150 °C, P = 1. Panel a: CH_4 and O_2 flow rates. Panel b: H_2 and H_2O flow rates. Panel c: CO and CO_2 flow rates. Panel d: gas and surface temperature profiles.

reforming zone, the catalyst temperature decreases and is flattened, while the gas temperature increases, over that of the solid and finally the two temperatures match at the outlet of the monolith. It is worth noting that in this experiment the reactor was not perfectly adiabatic, and the thermal efficiency (defined as the ratio between the experimental temperature rise and the theoretical adiabatic temperature rise [10]) was 90%. A dissipation term (Eq. (6)) was included in the enthalpy balance of the gas phase in order to account for the heat losses. A global heat transfer coefficient ($h_{reactor}$) of 10 W/m^2/K was estimated by matching the calculated thermal efficiency to the experimental one.

$$\dot{Q}_{lost} = \int_{z_0}^{z_{out}} h_{reactor} \cdot (T_{gas}(x) - T_{room}) \cdot \pi \cdot D_{reactor} \cdot dx \qquad (6)$$

Within the catalyst volume, the simulated curves closely match the measured profiles. For both phases, the position and the value of the maximum temperature are correctly predicted, with a small overestimation (35 °C) in the case of the gas profile. Differences are observed in the front heat shield in the temperature of the solid, which are probably associated with the uncertainty in the effective conductivity of α-Al_2O_3 and with possible drawbacks in the measurement technique. Smaller deviations are also present in the thermocouple measurement, which are likely associated with conduction and radiation errors (see Section 4.2).

3.4. Model simulations for the Rh-wc catalyst

When the washcoat was applied to the Rh catalyst, a remarkable increase in the activity was observed. The addition of the washcoat (Fig. 4) allowed the reaction to reach the thermodynamic equilibrium at the outlet of the catalyst. The extent of the oxidation zone kept unaltered, in line with the mass transfer limitation on the consumption of O_2 (see next section). The evolution of the species took place within one-third of the catalyst volume (0–4 mm along the axis), indicating that some reforming activity was ongoing also in the oxidation zone. Consequently, the chemical quenching associated with the promotion of the endothermic reforming reactions lowered the temperatures of the solid and of the gas compared to the Rh sample. Indeed, the average temperatures were 50–100 °C lower and the hot spot of the solid shifted closer to the inlet section of the monolith.

Even in the presence of such a strong modification of the activity, the model predicts well the observed features in terms of species profiles and outlet performances (Table 4). On the one hand, the agreement with the outlet performances is dictated by

Table 4
5 wt% Rh/2 wt% γ-Al_2O_3/α-Al_2O_3 catalyst: comparison between experimental and calculated outlet molar flows and temperature.

	CH_4 (mmol/s)	H_2 (mmol/s)	CO (mmol/s)	H_2O (mmol/s)	CO_2 (mmol/s)	T_{OUT} (°C)
Exp.	0.16	1.16	0.52	0.11	0.07	665
Calc.	0.17	1.13	0.54	0.09	0.07	640

the thermodynamic consistency of the C_1 scheme. On the other hand, the correct representation of the species profiles validates the model kinetics probed by the change in dispersion and remarks the fundamental importance of performing spatially resolved experiments. In line with the results obtained for the Rh catalyst, differences between the calculated and the experimental curves are present in the distribution of the products suggesting again an overestimation of the WGS activity. However, these deviations are less marked than in the case of the Rh-coated foam. Deviations are also apparent between 2 and 4 mm of the monolith, where a steep slope is observed in the evolution of the species up to the equilibrium: however, the data likely indicate the fine structure of the catalyst, that is, a local variation of the flow pattern due to the particular structure of the foam, which has not been accounted for by the model. An irregular distribution of the pore network has been clearly shown in Ref. [13].

The temperature profile of the solid and of the gas phase are matched (Fig. 4d): again, the position and the value of the maxima are correctly predicted, with less than 20 °C difference for the solid and an overestimation of 40 °C for the gas. In this experiment, the reactor was adiabatic (97% thermal efficiency) and no heat dissipation was included in the model.

4. Discussion

The numerical results, reported in the previous section, show that spatially resolved CH_4 CPO experiments could be well captured by a C_1 microkinetic scheme [16] and a 1D heterogeneous reactor model [19] using independent experimental estimates of the catalyst metal surface area and recent correlations for mass and heat transfer in foams [29]. In particular, the simulations show that the detailed mechanism is capable of covering almost one order of magnitude variation in the dispersion of Rh (74 vs. 630 cm^2/g_{Foam}). Considering that such conditions correspond to extremely low dispersion values (0.03% and 0.3%) and that the scheme was originally tuned using data with a 5% dispersed catalyst [27], two orders of magnitude dispersion were in principle covered. In this respect, it is worthy to note that, due to the large size of the Rh particles, possible structure sensitivity effects were minimized.

In this section, we aim at critically analyzing the results and comparing experiment and model results. First, we evaluate the impact of the real structure of the foam on the interpretation of the results, by exploring the sensitivity with respect to both its geometrical structure and conductivity. Then, we apply the reaction path analysis (RPA) to reveal the main reaction pathways that govern conversion and selectivity along the axial coordinate.

4.1. Sensitivity analysis on the pore diameter of the foam

In agreement with several works on short contact time CPO over Rh/α-Al_2O_3 catalysts [7,9,11,15,19,36], the experimental results confirm that the consumption of O_2 is mass transfer controlled: a ninefold increase in the metal area did not influence the length and the evolution of the O_2 consumption curves. As a consequence, the goodness of the model fit exclusively depends on the accuracy of the transport correlations and on the estimation of the geometrical properties of the foam, namely the geometric area, the pore diameter and the void fraction.

Fig. 5a provides a direct comparison between experiments and model predictions for both the catalysts. As expected, the calculated curves overlap: indeed, the mass transfer coefficients and consequently the length of the oxidation zone are a weak function of the gas temperature ($z_{ox} \sim T^{0.3}$ [7]), and the influence of the different temperature gradients on the transport rate is negligible. The simulations nicely describe the initial part (0–1 mm) of the experimental profiles (also overlapped), but less so in the last part of the oxidation zone. In the case of Rh-wc sample, the model approaches the data closer due to a local irregularity of the measured profile; though up to 1.1 mm, the slope of the curve was identical to that of the Rh sample. It is evident that the evolution of the measured O_2 concentration had a much steeper trend than the model curves, which follow instead a smooth exponential decay. A sensitivity analysis on the pore diameter was performed by simulating a foam with pore size of 325 μm (close to the nominal value of 317). Results are reported in Fig. 5. Fig. 5a in particular shows that the final part (between 1 and 2 mm) of the measured O_2 profile can be better described assuming smaller pores. However, due to the increase in the mass and heat transfer rate, the initial consumption of O_2 (between 0 and 1 mm) is overpredicted. Besides, Fig. 5b shows that also the calculated temperature profiles tend to overpredict the measured ones; when assuming smaller pores, the enhanced rate of O_2 mass transfer results in an increased calculated surface hot spot temperature, while the enhanced rate of heat transfer results in increased calculated gas-phase temperature, respectively.

These results suggest that the internal structure of the foam influences the consumption profile. As discussed in [13], blocked pores can hinder the radial mixing, giving rise to irregular flow pat-

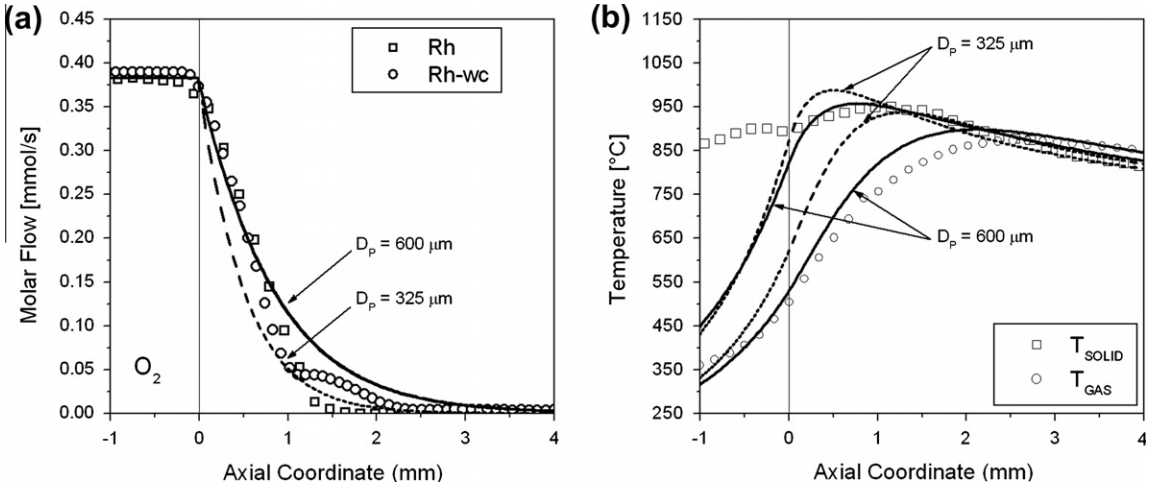

Fig. 5. Comparison between model prediction (solid lines) and data (symbols) for different pore diameters (— 600 μm; - - - 325 μm). Panel a: consumption of O_2. Panel b: gas and surface temperature profiles for the 5 wt% Rh catalyst.

terns. Based on the data reported for analogous CH_4 CPO experiments over 80 ppi α-Al_2O_3 foams, the length of the oxidation zone varies between 1.3 mm [7] and 2 mm [12], this range being comparable to the diameter of one pore. The measured, non-exponential steep decay could then be due to a local decrease in the pore diameter toward the inner part of the foam. Note that the variability of the pore diameter examined in Fig. 5 is well within the range of pore diameters shown by Fig. 1.

4.2. Sensitivity analysis on the conductivity of α-Al_2O_3

One of the most important pieces of information provided by the spatially resolved measurements is the knowledge of the temperature profile of the catalytic surface. In order to rationalize the design of a CPO reformer, the correct prediction of the position and the value of the hot spot on the surface is crucial. As discussed, the model quantitatively predicts the temperature of the gas and the solid within the catalyst (Fig. 3d and Fig. 4d). Nonetheless, looking at the temperature of the solid, a significant difference is apparent in the front heat shield (FHS). Back dispersion effects, i.e., heat conduction through the monolith to the inert shield, have been previously reported to significantly decrease the hot spot and benefit the catalyst life-time [4,36]. The model accounts for the axial conduction of heat and for the effect of radiation on the conductivity of the alumina support. The results of a sensitivity analysis on this parameter are reported in Fig. 6 for Rh-wc: along with Refs. [13,12], the conductivity of polycrystalline aluminum oxide was assumed for the foam, with values between 16 W/m/K (k_{Al2O3} at ~350 °C) and 6.5 W/m/K (k_{Al2O3} at ~950 °C). In the FHS, the measured solid temperature cannot be described even with the highest value of k_{Al2O3}, while, as expected, the gas temperature is overestimated with increasing k_{Al2O3}. Additionally, in increasing conductivity, the hot spot of the solid is underestimated and the gas temperature overestimated. Considering that the foam struts are porous and partially empty, it is reasonable that the effective conductivity is lower than that of bulk alumina: with a value of 2 W/m/K, the maxima and the thermocouple measurements are best described.

The present analysis also suggests that the pyrometer measurements within the blank support could be affected by artifacts due to the optical acceptance of the fiber probe from the glowing front face of the catalyst, which resulted in an overestimation of the real temperature.

Indeed, if a heat exchange coefficient between the solid surface and the gas in the FHS were estimated on the basis of the measured temperatures, such coefficient would result much smaller than that predicted by the theoretical transport correlation herein adopted. Indeed, within the first 9 mm of the FHS, the estimated coefficient ranges between 3 and 21 W/m^2/K while the theoretical coefficient amounts to 110–130 W/m^2/K. On the other hand, when crossing the catalyst inlet section, the experimental coefficient well agrees with the theoretical value. This pieces of evidence further confirm that the pyrometer measurement within the FHS is biased by optical artifacts.

To complete the critical analysis of the temperature measurements, we observe that underestimation of the gas temperature by the thermocouple cannot in principle be ruled out. As discussed in Ref. [4], conduction errors explain the underestimation of the hot spot temperature for a thermocouple entering the monolith from the front.

4.3. Surface coverage and reaction path analysis

Recently, Maestri et al. [15] has reported that, within a quasi-isothermal catalytic chamber, CH_4 CPO on Rh exhibits up to three different regimes, which establish along the catalyst bed: deep combustion of methane; direct formation of syngas in parallel with catalytic combustion of hydrogen; reforming, when oxygen is no longer available. In this section, we attempt to extend and validate under adiabatic conditions the mechanism analysis of Ref. [15].

Fig. 7 reports the calculated profiles of the molar fractions of the reactants at the gas–solid interface and in the bulk of the gas phase (Panels a and b). The coverage fractions of Rh-free sites and of the adsorbed intermediates are reported in Panels c and d. The concentration of O_2 at the gas–solid interface drops to zero since the very inlet of the catalyst, while O_2 is present in the bulk of the gas phase and gradually decreases within the oxidation zone.

This finding points out that O_2 consumption is strictly mass transfer limited along all the axial coordinate. On the other hand, the reforming zone is only partially governed by the diffusion of CH_4, consistently with the sensitivity of the model to the metal surface area. Due to the coupling of high temperatures and zero concentration of O_2 at the interface, the metal surface is essentially clean along the whole catalyst length. Free Rh sites dominate, decreasing from 86% to 60% in the case of Rh (Fig. 7c) and from 75% to 42% on the Rh-wc catalyst (Fig. 7d). Besides Rh sites, H adatoms (~30% at the outlet on both samples) and CO* molecules (~9% on Rh and ~18% on Rh-wc) are the most abundant reactive intermediates, followed by CH* (~1% on Rh, ~8% on Rh-wc), CH_2*, OH* and C* species. Overall, in line with the lower surface temper-

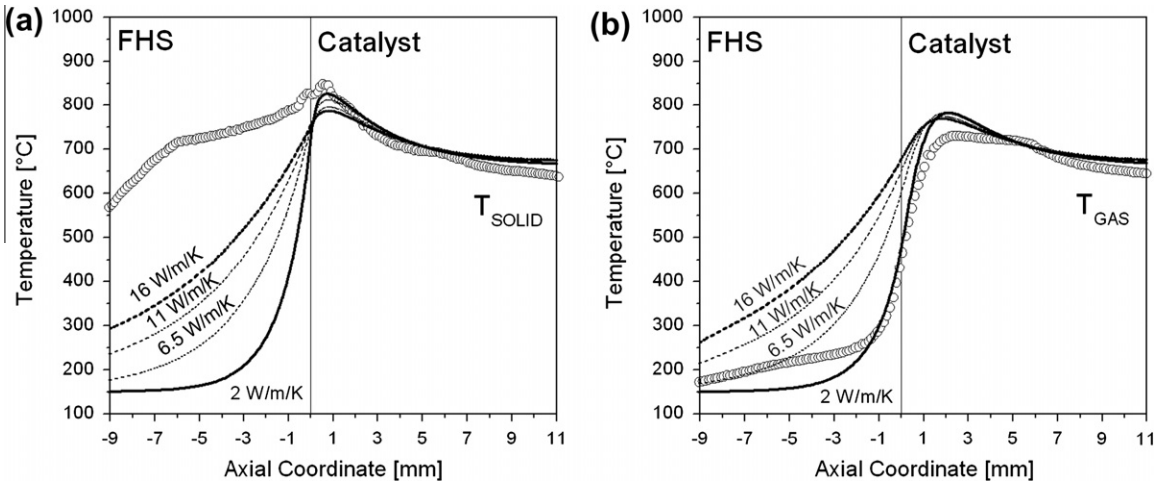

Fig. 6. Comparison between model prediction (solid lines) and data (symbols) for different thermal conductivity values of α-Al_2O_3 [42]. Panel a: temperature profile of the solid phase. Panel b: temperature profile of the gas phase. 5 wt% Rh/2 wt% γ-Al_2O_3 catalyst.

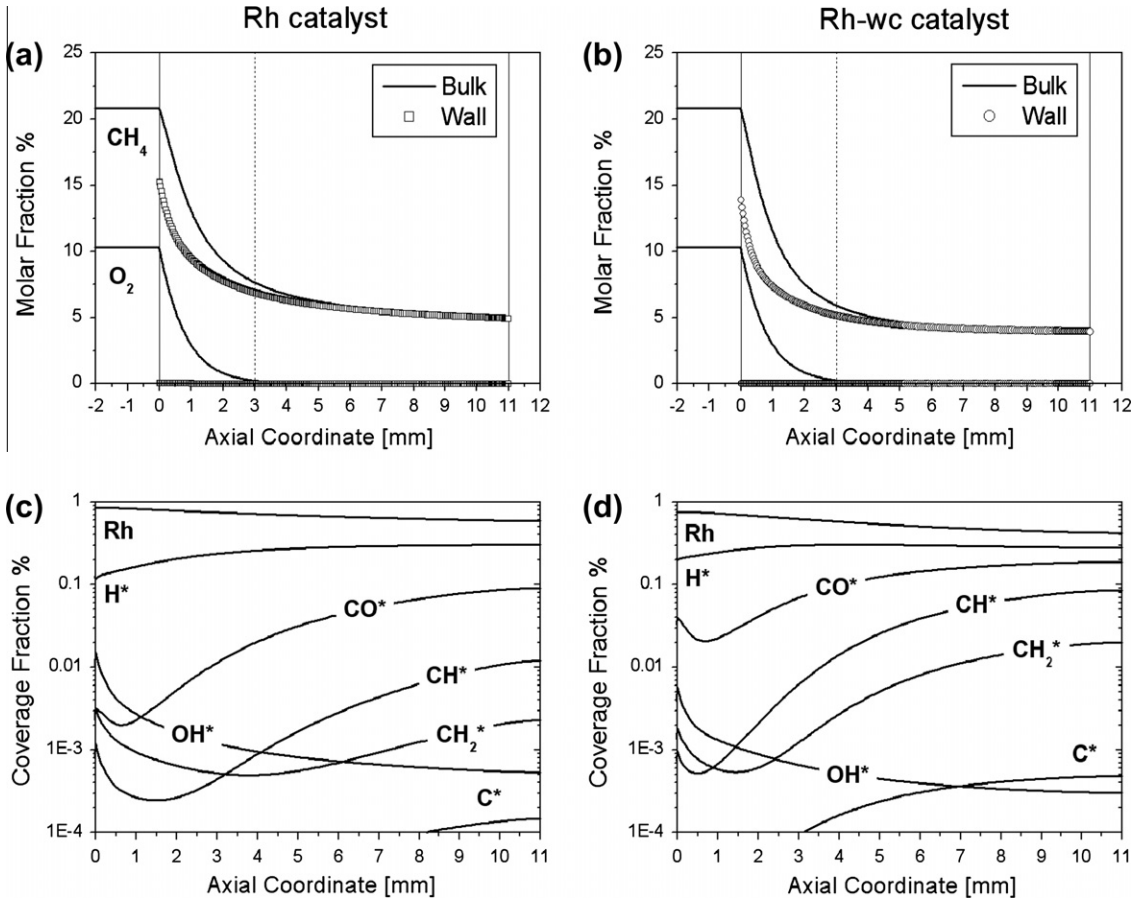

Fig. 7. Molar fractions of CH_4 and O_2 in the bulk of the gas phase and at the catalyst wall, and dominant surface coverage along the axis of the catalyst. Panels a and c: 5 wt% Rh. Panels b and d: Panel d: 5 wt% Rh/2 wt% γ-Al_2O_3.

atures, higher fractions of adspecies are found on the washcoated sample compared to the Rh sample.

RPA reveals that the main routes of products are in line with Regime II and Regime III, reported by Maestri et al. [15]. In the zone of the reactor where O_2 and syngas coexist, Regime II occurs: CH_4 is consumed via a surface pyrolytic route with progressive removal of H according to $CH_x^* + * \rightarrow CH_{x-1}^* + H^*$. The carbon adatom C^* is removed from the surface by reaction with OH^* ($C^* + OH^* \rightarrow CO^* + H^*$) and desorbs as CO or CO_2 ($CO^* + OH^* \rightarrow CO_2^* + H^*$) depending on the local WGS equilibrium.

In the oxidation zone, most of OH^* is consumed by the reaction with C^* and CO^* and the rest by the reaction between OH^* and H^* to give H_2O^*. This result seems to indicate that the overestimation of the H_2 production (Section 3.3 of the present paper) in the oxidation zone (Regime II, as in Ref. [15]) could be related to the overestimation of the consumption of OH^* via C^* and CO^* ("WGS route"). As reported in Fig. 3b of Ref. [15], overestimation of OH^* consumption by C^* and CO^* results in an underestimation of H_2O^* production ($OH^* + H^* \rightarrow H_2O^*$). Consequently, a higher ratio of the H^* formed on the surface by the CH_4 pyrolysis desorbs in the gas phase.

Due to the presence of O_2 in the bulk of the gas phase, OH^* forms via reaction between O_2 leaking to the surface and H^* atoms. H^* either recombines with OH^* and desorbs as H_2O, or recombines with another H^* and desorbs as H_2. The overall molecular stoichiometry is a combination of steam reforming, H_2 combustion and WGS, meaning that also in the oxidation zone H_2 and CO do not form directly from the reaction of CH_4 and O_2, in line with what reported in Ref. [15].

In the reforming zone (Regime III [15]), O_2 is absent in the gas phase, but the reaction path is almost identical to that of the oxidation zone; the only difference being that the OH^* intermediates originate from adsorption and dissociation of H_2O ($H_2O^* + * \rightarrow OH^* + H^*$). In this case, the overall molecular stoichiometry can be represented as a simple combination of SR and WGS. The CO_2-reforming reaction does not play any role, and the variations in the CO_2 profile are due exclusively to the WGS reaction, as also observed in [11,28].

A key observation of the model analysis is that the main oxidizer is OH^* rather than O^* even under adiabatic conditions, as reported in Refs. [15,18]. This is different from most of the mechanisms reported in the literature. Both in experimental and in theoretical analyses (e.g., [14,37–41]), it is usually assumed that the main oxidizer is O^* ignoring the carbon oxidation via OH^*. In this respect, the fact that the model is single site is not believed a major limitation; oxygen is assumed to adsorb over the most energetically stable site, which is the case of interest at very low O^*-coverage. Overall, these results confirm that the isothermal analysis of the CPO mechanism reported in [15] applies under adiabatic conditions as well. In particular, this analysis stresses that under steady-state conditions, the O_2 consumption is always mass transfer limited (Regime II dominates over Regime I [15]). Consequently, the tailoring of the geometry of the catalyst support can be effectively employed in order to properly dose O_2 (and consequently the heat release) along the axial coordinate. This, as showed in Refs. [4,15], can lead to a proper reduction of the local hot spot with a beneficial effect on the catalyst stability and durability [5].

5. Conclusions

In this work, we have presented the microkinetic analysis of spatially resolved autothermal CH_4 CPO experiments over 5 wt% Rh-coated 80 ppi α-Al_2O_3 foams with and without washcoat [10]. The characterization of the catalysts revealed a nearly one order of magnitude increase in metal surface area upon addition of the washcoat (74 vs. 630 cm^2/g_{Foam}). Differently from previous work in the field, a fully predictive approach was adopted in the numerical analysis by introducing in the model the experimentally estimated catalyst metal surface area and state of the art correlations for heat and mass transfer in foams.

As a result, the microkinetic model [16] was able to quantitatively account for the axial evolution of the species and to accurately predict gas and surface temperature profiles within the catalyst volume. Remarkably, the model was able to describe with satisfactory accuracy the spatial resolution of reactants and products for two different catalyst loadings, using the measured catalyst dispersion as an independent input.

The comparison between model predictions and experimental results suggests also that further analysis is needed concerning the WGS of the C_1 microkinetic scheme and that artifacts possibly bias the measurement of the surface temperature outside the catalytic volume when an optical pyrometer is used.

Concerning the reaction mechanism, analysis of the reaction pathways allowed to highlight that under adiabatic conditions CH_4 CPO proceeds exclusively according to Regime II and Regime III reported in Ref. [15], confirming on a more general basis the mechanistic analysis of Ref. [15]. This means that O_2 consumption is strictly governed by mass transfer along the axial coordinate and co-presence of O_2 and syngas in the bulk of the gas phase is only due to mass transfer limitations. CH_4 is activated via pyrolytic decomposition. A key observation of the model analysis is that the main oxidizer is OH^* rather than O^* even under adiabatic conditions. In the oxidation zone (Regime II), OH forms by the reaction of O^* and H^* adatoms, while in the reforming zone (Regime III), OH^* forms from H_2O dissociation.

On a more general basis, the present results emphasize the importance of modeling spatially resolved experiments in order to gain insights into the complexity of a process and enable fundamental understanding of the underlying phenomena at different time and space scales.

References

[1] D.A. Hickman, L.D. Schmidt, Journal of Catalysis 138 (1992) 267–282.
[2] A.L. Dicks, Journal of Power Sources 61 (1996) 113–124.
[3] C.G. Bauer, T.W. Forest, International Journal of Hydrogen Energy 26 (2001) 55–70.
[4] A. Beretta, G. Groppi, M. Lualdi, I. Tavazzi, P. Forzatti, Industrial and Engineering Chemistry Research 48 (2009) 3825–3836.
[5] I. Tavazzi, A. Beretta, G. Groppi, M. Maestri, E. Tronconi, Catalysis Today 129 (2007) 372–379.
[6] R. Horn, N.J. Degenstein, K.A. Williams, L.D. Schmidt, Catalysis Letters 110 (2006) 169–178.
[7] R. Horn, K.A. Williams, N.J. Degenstein, A. Bitsch-Larsen, D.D. Nogare, S.A. Tupy, L.D. Schmidt, Journal of Catalysis 249 (2007) 380–393.
[8] A. Bitsch-Larsen, N.J. Degenstein, L.D. Schmidt, Applied Catalysis B: Environmental 78 (2008) 364–370.
[9] A. Bitsch-Larsen, R. Horn, L.D. Schmidt, Applied Catalysis A: General 348 (2008) 165–172.
[10] A. Donazzi, B.C. Michael, L.D. Schmidt, Journal of Catalysis 260 (2008) 270–275.
[11] B.C. Michael, A. Donazzi, L.D. Schmidt, Journal of Catalysis 265 (2009) 117–129.
[12] R. Horn, K.A. Williams, N.J. Degenstein, L.D. Schmidt, Journal of Catalysis 242 (2006) 92–102.
[13] D. Dalle Nogare, N.J. Degenstein, R. Horn, P. Canu, L.D. Schmidt, Journal of Catalysis 258 (2008) 131–142.
[14] R. Schwiedernoch, S. Tischer, C. Correa, O. Deutschmann, Chemical Engineering Science 58 (2003) 633–642.
[15] M. Maestri, D.G. Vlachos, A. Beretta, P. Forzatti, G. Groppi, E. Tronconi, Topics in Catalysis 52 (2009) 1983–1988.
[16] M. Maestri, D.G. Vlachos, A. Beretta, G. Groppi, E. Tronconi, AIChE Journal 55 (2009) 993–1008.
[17] M. Maestri, A. Beretta, T. Faravelli, G. Groppi, E. Tronconi, D.G. Vlachos, Chemical Engineering Science 63 (2008) 2657–2669.
[18] M. Maestri, D.G. Vlachos, A. Beretta, G. Groppi, E. Tronconi, Journal of Catalysis 259 (2008) 211–222.
[19] M. Maestri, A. Beretta, G. Groppi, E. Tronconi, P. Forzatti, Catalysis Today 105 (2005) 709–717.
[20] I. Tavazzi, M. Maestri, A. Beretta, G. Groppi, E. Tronconi, P. Forzatti, A.I.Ch.E. Journal 52 (2006) 3234–3245.
[21] J. Kong, A.J. Shih, SAE paper, 2004-01-0962, 2004, pp. 1–14.
[22] A. Frassoldati, T. Faravelli, E. Ranzi, International Journal of Hydrogen Energy 31 (2006) 2310–2328.
[23] O. Deutschmann, L.D. Schmidt, AIChE Journal 44 (1998) 2465–2477.
[24] J.G. Fourie, J.P. Du Plessis, AIChE Journal 50 (2004) 547–556.
[25] A.B. Mhadeshwar, H. Wang, D.G. Vlachos, Journal of Physical Chemistry B 107 (2003) 12721–12733.
[26] A.B. Mhadeshwar, D.G. Vlachos, Journal of Physical Chemistry B 109 (2005) 16819–16835.
[27] A. Donazzi, A. Beretta, G. Groppi, P. Forzatti, Journal of Catalysis 255 (2008) 241–258.
[28] A. Donazzi, A. Beretta, G. Groppi, P. Forzatti, Journal of Catalysis 255 (2008) 259–268.
[29] G. Incera Garrido, F.C. Patcas, S. Lang, B. Kraushaar-Czarnetzki, Chemical Engineering Science 63 (2008) 5202–5217.
[30] L. Giani, G. Groppi, E. Tronconi, Industrial and Engineering Chemistry Research 44 (2005) 4993–5002.
[31] G. Groppi, L. Giani, E. Tronconi, Industrial and Engineering Chemistry Research 46 (2007) 3955–3958.
[32] T.B. Sweeting, D.A. Norris, L.A. Strom, J.R. Morris, Materials Research Society Symposia Proceedings 368 (1995) 309.
[33] N.J. Degenstein, R. Subramanian, L.D. Schmidt, Applied Catalysis A: General 305 (2006) 146–159.
[34] T. Sanders, P. Papas, G. Veser, Chemical Engineering Journal 142 (2008) 122–132.
[35] A. Beretta, A. Donazzi, G. Groppi, P. Forzatti, V. Dal Santo, L. Sordelli, V. De Grandi, R. Psaro, Applied Catalysis B – Environmental 83 (2008) 96–109.
[36] M. Bizzi, G. Saracco, R. Schwiedernoch, O. Deutschmann, AIChE Journal 50 (2004) 1289–1299.
[37] A.M. Efstathiou, A. Kladi, V.A. Tsipouriari, X.E. Verykios, Journal of Catalysis 158 (1996) 64–75.
[38] A. Erdohelyi, J. Cserenyi, F. Solymosi, Journal of Catalysis 141 (1993) 287–299.
[39] J.M. Wei, E. Iglesia, Journal of Catalysis 225 (2004) 116–127.
[40] G. Jones, J.G. Jakobsen, S.S. Shim, J. Kleis, M.P. Andersson, J. Rossmeisl, F. Abild-Pedersen, T. Bligaard, S. Helveg, B. Hinnemann, J.R. Rostrup-Nielsen, I. Chorkendorff, J. Sehested, J.K. Norskov, Journal of Catalysis 259 (2008) 147–160.
[41] D.o.E., USA, Hydrogen, Fuel Cells and Infrastructure Technologies program, 2008. <http://www1.eere.energy.gov/hydrogenandfuelcells/production/natural_gas.html>.
[42] F.P. Incropera, D.P. DeWitt, T.L. Bergman, A.S. Lavine, Fundamentals of Heat and Mass Transfer, 6th ed., Wiley, New York, 2007.